


# INTERMITTENT LOW-FREQUENCY EXPERIMENTAL CAVITY DYNAMICS

Jesse McCarthy[1], Connor Marshall[1], Christopher Brown[1,2] & Malcolm Jones[1]

[1]Platforms Division, Defence Science and Technology Group, Fishermans Bend, VIC 3207, Australia
[2]School of Engineering, RMIT University, Melbourne, VIC 3000, Australia

## Abstract

Aircraft cavities for stores (e.g. munitions) generate acoustics that affect the release response of stores. The low-frequency (LF) bandwidth of cavity acoustic spectra has received relatively little attention compared with the well-established Rossiter modes. In this study, the coherency and intermittency of the LF bandwidth—characterised by temporal switching between active and inactive states—are shown to be at least as important to understand as the Rossiter resonances. This importance is underscored by recent findings from Marshall et al. [1], obtained under flight-representative conditions, which demonstrated that LF dynamics can induce significant spatio-temporal pressure variations within the cavity, potentially leading to non-repeatable store-release trajectories. A comprehensive experimental dataset of an empty rectangular cavity [2, 3] is re-examined, with particular emphasis on the LF bandwidth ($0.001 \leq \mathrm{St}_L \leq 0.02$, where $\mathrm{St}_L$ is the Strouhal number based on cavity length). The analysis spans a range of free-stream Mach numbers, cavity yaw angles, and intra-cavity measurement locations. In addition to uncovering previously unreported features, the results reveal a pronounced spatio-temporal dependence of the LF bandwidth, corroborating the findings in [1] and reinforcing the importance of resolving this bandwidth. Accordingly, these findings indicate that experimental and computational sampling periods should be defined based on LF bandwidth resolution rather than the lowest Rossiter mode alone, as is common practice. Therefore, a methodology for determining an appropriate sampling period is proposed.

**Keywords:** unsteady, aero-acoustics, wavelet, coherence, intermittency

## 1 Introduction

The release of stores from an internal bay, or cavity, is a highly physics-rich yet practical challenge, and one that dates back to WWI when bombs were dropped from the Handley-Page Type-O aircraft. Open or transitional cavities[1] exposed to free-stream flow—particularly in the transonic regime—generate a highly coupled aero-structural-acoustic environment. When interacting with smaller or potentially aerodynamically unstable stores, accurate characterisation of these cavity dynamics is essential for predicting their influence on store release trajectories, both from fundamental and operational perspectives. Generally, a combination of high-fidelity scale-resolving computational fluid dynamics (SR-CFD), ground-based experimental (i.e. wind tunnel) testing and/or instrumented flight testing are required to fully capture the cavity-store time dependent behaviours. From these data, reduced-order models (ROM) are often derived based on a number of simplifying assumptions (e.g. [4, 5]), sacrificing accuracy in favour of workflow scalability and computational efficiency. Indeed, the quality of ROM predictions has an intricate nexus with the extent to which the higher fidelity methods have holistically resolved the cavity dynamics.

[1]That is, those with a length to depth ratio $L/D$ in the range $1 \lesssim L/D \lesssim 9$.

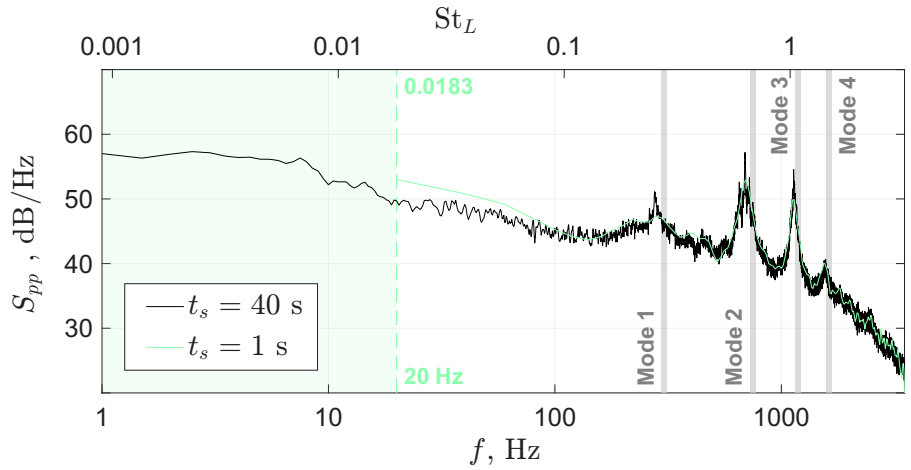



Figure 1 – Auto-spectral density (ASD) estimates, $S_{pp}$, of a pressure signature measured on the aft wall near the lip of a rectangular cavity, with $L/D = 5$ and at Mach 0.8 in the DSTG TWT [2]. The ASD estimates used different sample periods, $t_s$, of the pressure signature, and the predicted Rossiter modal frequencies according to [7] are overlaid for reference.

Since the seminal work of Coley and Lofthouse [6], the well-known cavity Rossiter modes [7] (also referred to as cavity resonances) have been the primary focus of investigation when it comes to understanding the store post-release trajectory. For open cavities, there are often 3 to 5 observable Rossiter modes in the cavity pressure signature, depending on specific cavity geometry and oncoming flow conditions. Shown in Figure 1 are two auto-spectral density (ASD) estimations of pressure fluctuations sampled at 7 kHz near the rear lip of an empty rectangular cavity, with length to depth ratio $L/D = 5$, at Mach 0.8, in the Defence Science and Technology Group (DSTG) Transonic Wind Tunnel (TWT) in Melbourne, Australia [2, 3]. The ASDs are plotted against dimensional frequency, $f$, as well as dimensionless Strouhal number, $\mathrm{St}_L = fL/U_\infty$, where $U_\infty$ is the free-stream flow velocity. Typically with high-fidelity simulations or measurements, the sample period is optimised to capture a limited number of oscillatory cycles of the lowest Rossiter mode, while avoiding excess computational burden or resource expenditure. The first ASD (black) is estimated from the full 40 s pressure time trace. The second ASD (green) uses a 1 s sample ($\sim 300$ cycles of the lowest Rossiter mode), typical of SR-CFD run-times or commercial wind tunnel sampling periods. As noted in [1, 8], ASD estimation can introduce bias error, so both ASDs were estimated using the same algorithm (Welch's method [9]), window function (Nuttall symmetric [10]), overlap (70.5%) and number of ensemble averages (20). This results in ASDs that are statistically equivalent, but possess highly disparate resolution bandwidths.

Immediately noticeable in the ASD using a sample period $t_s = 1$ s is the loss of spectral resolution. The dominant Rossiter mode magnitudes differ by as much as 3 dB/Hz compared to the long-period ASD estimate; but more importantly, the obfuscation (or even loss) of low-frequency (LF) information, where $0.001 \lesssim \mathrm{St}_L \lesssim 0.02$, is evident. In Figure 1, this bandwidth contains spectral power in the order of the dominant Rossiter mode, yet it is broadband in nature as there are no discernible peaks (or tones) and is thus easily overlooked or dismissed as irrelevant—especially when spectral quantities are plotted against a linear abscissa scale. Furthermore, in a cavity-stores context, these larger spatio-temporal flow scales are seldom investigated due to the expenses required for a comprehensive exposition, and also because of the widely-held assumption that Rossiter modes dominate the store trajectory post-release [4, 6, 8]. Despite a limited number of fundamental studies—such as those of [11, 12, 13]—that have mentioned or even highlighted the LF cavity dynamics, their underlying physical mechanisms, scaling laws, and moreover their relationship with post-release store dynamics, remain the most under-characterised aspect of cavity flows [14], necessitating a greater understanding the LF bandwidth.

Recently, Marshall et al. [1] showed that the time scale of a store traversing the cavity shear layer can be on the order of the half-period of LF pressure fluctuations. These fluctuations are aperiodic

and impulsive, making ROM-based trajectory predictions difficult because they violate assumptions of 1) statistical stationarity, 2) periodicity, and 3) Rossiter-mode-dominated dynamics (e.g. [4, 15]). The datasets previously published by [2, 3] contained a detailed evaluation of the effects of cavity $L/D$, yaw angle, Mach and Reynolds numbers, and inner geometry, on Rossiter mode modulations. Long sample periods, i.e. 40 s as previously shown in Figure 1, were acquired—not for study of the LF dynamics, but rather to ensure statistical convergence of the cavity Rossiter modes, referred to by [8] in more recent work as the 'mature cavity' condition. Nevertheless, these long sample periods are useful for resolving the LF bandwidth. Thus, the central theme of this work is to revisit a subset of this dataset; but this time, in a time-dependent context and with a focus on the LF characteristics of the cavity pressure signature. Naturally, the ASD is by itself an insufficient metric for this task; instead, the wavelet transform is used, similarly to [16]. The intention is to catalyse discussion surrounding the inclusion of LF cavity dynamics in SR-CFD, experimental testing, and ROM-based analysis and clearance/certification workflows.

## 2 Overview of Wavelet Analysis

### 2.1 The Wavelet Transform

The wavelet transform, as applied to the analysis and feature extraction of fluidic flows and turbulence, has existed since the late 1980s [17]. Torrence and Compo [18] in 1998 were among the first to give a comprehensive overview of wavelet analysis from a practical perspective, and the reader is referred to their work for a detailed overview of the underpinning theory. Key concepts pertaining to the forthcoming analysis are covered in brief.

The wavelet transform is a time-localised, scale independent method of decomposing a transient signal (or signals). It differs from traditional Fourier analysis in that a fixed window size—required to satisfy the periodicity constraint of the Fourier transform—is not required, and instead each scale (or mode) is treated independently in time through convolution with a translated and dilated version of a 'mother' waveform, the wavelet basis function. In this sense, wavelet analysis is much akin to use of a bandpass filter bank, each with different passband frequencies. Here, the Morlet wavelet basis is used, similar to the analysis of Bacci et al. [16] and use in the authors' previous work [19, 20], but moreso as recommended by [18] for feature extraction purposes. The Morlet wavelet basis is a complex plane wave, containing both magnitude and phase information, modulated by a Gaussian function,

$$\psi_0 = \pi^{-1/4} \cdot e^{i\omega_0 \eta} \cdot e^{-\eta^2/2}, \tag{1}$$

where $i = \sqrt{-1}$, $\eta$ is non-dimensional time and $\omega_0$ is the Morlet centre frequency, taken (in this case) to be 6 to satisfy the admissibility condition[2] as per [17, 18]. Then, a family of 'child' wavelets $\psi(\eta)$ derived from the basis function are defined as

$$\psi(\eta) = \psi_0 \left( \frac{\eta - \tau}{a} \right), \tag{2}$$

where $\tau$ is the local time index (i.e. the translation parameter) and $a$ is the wavelet scale (i.e. dilatation parameter). Finally, the wavelet transform represents a convolution of all translated and dilated wavelets with transient signal $x(t)$, over all time; viz.

$$W_{xx} = \frac{1}{\sqrt{a}} \int_{-\infty}^{\infty} x(t) \cdot \psi^* \left( \frac{t - \tau}{a} \right) dt, \tag{3}$$

where the asterisk denotes the complex conjugate (or time-reversed) value. Most often, for reasons of efficiency, the convolution in Equation (3) is carried out in the Fourier domain and in discrete form [18]. Equation (3) is the most basic time-frequency analysis tool used to unravel the transient behaviour of pressure fluctuations measured at a single cavity location. However, to understand spatially-varying correlations one must extend Equation (3) to the cross-wavelet transform, $W_{xy}$, which is defined as

$$W_{xy} = W_{xx} \cdot W_{yy}^*, \tag{4}$$

[2]Note this differs from Bacci et al. [16], who took $\omega_0 = 10$ but provided no explanation or justification for this choice.

where $W_{yy}$ is the wavelet transform of transient signal $y(t)$ according to Equation (3). From this, Torrence and Webster [21] defined a wavelet coherence, $R^2_{xy}$ as a function of wavelet scale,

$$R^2_{xy} = \frac{\left|\left\langle a^{-1} W_{xy} \right\rangle\right|^2}{\left\langle a^{-1}\left|W_{xx}\right|^2\right\rangle \left\langle a^{-1}\left|W_{yy}\right|^2\right\rangle}, \tag{5}$$

where the angled brackets denote smoothing in time and scale, and the factor $a^{-1}$ converts the quantities to energy densities, so that $0 \leq R^2_{xy} \leq 1$ as with the Fourier-based ordinary coherence function [22].

The wavelet quantities in Equations (3) to (5) have been shown to be consistent estimators of their Fourier equivalents [18, 21], and hence their time-integrated values are smoothed representations of the corresponding Fourier quantities. For instance, the auto wavelet power (AWP) and cross wavelet power (CWP) are defined as per Equations (6) and (7) respectively:

$$W_{XX} = \left|W_{xx}\right|^2 \tag{6}$$

$$W_{XY} = \left|W_{xy}\right|. \tag{7}$$

Then, by taking the mean value over the total sample period $t_s$ one obtains the global AWP, CWP or wavelet coherence:

$$\hat{W}_{XX} = \frac{1}{t_s}\int_0^{t_s} W_{XX}\, dt \tag{8}$$

$$\hat{W}_{XY} = \frac{1}{t_s}\int_0^{t_s} W_{XY}\, dt \tag{9}$$

$$\hat{R}^2_{xy} = \frac{1}{t_s}\int_0^{t_s} R^2_{xy}\, dt. \tag{10}$$

Note that the global quantities in Equations (8) to (10) are not utilised for the remainder of this study, and are included here for reference only.

Finally, it is important to note the relationship between Morlet wavelet scale, $a$, and Fourier frequency $f$; for $\omega_0 = 6$ in Equation (1) [18],

$$a = 0.971 \cdot f, \tag{11}$$

and so wavelet scales are plotted using $f$ instead of $a$, as typically done with Fourier-based quantities.

## 2.2 Significance Testing

In order to draw meaningful conclusions from wavelet analysis, it is imperative that detected features are significance tested against a known probability distribution function (PDF) [18]. Peaks in wavelet quantities are typically tested for significance against white-noise (i.e. a Gaussian or random process) or red-noise (i.e. an auto-regressive or Markov process) power spectra [18]. If it is assumed that the wavelet coefficients, which are complex-valued for the Morlet basis, are normally distributed then the squared value (Equation 6) are chi-square ($\chi^2_2$) distributed with 2 degrees of freedom. Following [18], the 95% confidence level, or 5% significance level, of the AWP can then be determined using a red-noise background spectrum[3] as the null hypothesis $H_0$,

$$\frac{W_{XX}}{\sigma^2_x} \Rightarrow \frac{1}{2} S_{zz} \chi^2_2, \tag{12}$$

where $\Rightarrow$ means 'is distributed as',

$$S_{zz} = \frac{1-\gamma^2}{1+\gamma^2-\cos(2\pi k/N)}, \tag{13}$$

[3] A red-noise spectrum is characterised by high power at low frequencies, with decreasing power as frequency increases. It is a suitable choice to model many physical process, especially in fluid dynamics where energy scales typically cascade through viscous dissipation and momentum transfer—see also McCarthy et al. [20].

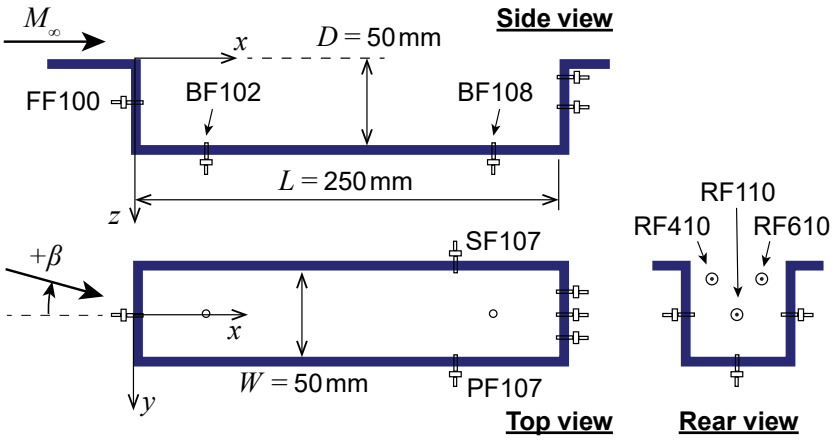



Figure 2 – Relevant cavity analysis parameters, adapted from [2]. Pressure measurement locations are: RF = Rear face, BF = Bottom face, FF = Front face, SF = Starboard face, PF = Port face.

$\sigma_x^2$ is the variance, $0 \leq \gamma \leq 1$ is the lag-1 autocorrelation coefficient ($\gamma = 0$ corresponds to a white-noise process), $k$ is frequency index and $N$ is the number of spectral lines. So, by normalising the AWP by the time-series variance, the 95% confidence level of peaks in AWP can be established as a function of time and frequency using Equations (12) and (13) with a suitable choice of $\gamma$ [23]. In essence, this process measures peaks in AWP relative to a best-fit red noise spectrum. Similarly, for significance testing peaks in CWP between two time series, each with background red-noise spectra $S_{zz}^X$ and $S_{zz}^Y$ given by Equation (13), the respective wavelet coefficients are chi-square distributed and thus it can be stated for the Morlet basis that

$$\frac{W_{XY}}{\sigma_x \sigma_y} \Rightarrow \frac{3.999}{2} \sqrt{S_{zz}^X S_{zz}^Y} \tag{14}$$

for a 95% confidence level as a function of time and frequency, through normalisation of the CWP by the product of standard deviations $\sigma_x$ and $\sigma_y$.

Significance testing for peaks in wavelet coherence has no closed analytical form as with the AWP and CWP. Instead, Monte-Carlo simulations must be performed by generating surrogate pairs of red-noise spectra, and computing the wavelet coherence between the two, as per [20, 21, 24]. Here, 1,000 surrogate pairs of background red-noise spectra are generated for each wavelet coherence computation, to determine the 95% confidence levels in time-frequency space, to ensure a statistically significant sample set as per [20].

## 3 Cavity Time-Frequency Analysis

The wavelet analysis techniques outlined in Section 2 are applied to data published in [2] and [3], focusing on the LF bandwidth of the cavity pressure signature. First, the effects of Mach number and cavity yaw angle are examined, for an empty rectangular $L/D = 5$ cavity configuration, using measurements on the aft wall near the lip of the cavity where pressure fluctuations are known to be most severe, possibly due to shear-layer impingement [12] or span-wise oscillation of the shear layer [13]. Then, cavity yaw angle is set to zero and spatial variations (and correlations) at a Mach number of 0.9 are evaluated. A schematic depicting the relevant analysis parameters is shown in Figure 2.

### 3.1 Oncoming Flow Dependence

The DSTG TWT has the capability to vary Mach number and Reynolds number ($\text{Re}_L = U_\infty L/\nu$ where $\nu$ is kinematic viscosity) independently through pressurisation or evacuation of the plenum chamber in which the working section is situated—for further details, refer to [2]. The work in [2] showed that variations in free-stream Reynolds number had negligible influence on the Rossiter modes; however, this effect could not be verified for the LF bandwidth, as a consistent set of sensor data were not available across the range of Reynolds numbers. So, the plenum total pressure, $P_0$, was set to 150 kPa, giving a $\text{Re}_L$ of order 5.1 million, with the Mach number $M_\infty$ varied in the range $0.5 \leq M_\infty \leq 1.1$ in steps of $\Delta M_\infty = 0.2$. The oncoming boundary layer was characterised and reported in [2]. Also,

cavity yaw angle[4] $\beta$ was varied in the range $0^\circ \leq \beta \leq 45^\circ$ with resolution $\Delta\beta = 5^\circ$. Pressure sensors RF410 and RF610 (Figure 2) were selected as they are symmetrically distributed about the cavity centre-line; thus, with only $\beta > 0^\circ$ it may reasonably be assumed that flow features are mirrored about the $x-z$ plane for $\beta < 0^\circ$.

The wavelet quantities are plotted in time-frequency space as follows: time is non-dimensionalised to convective units based on the cavity length as

$$\tau_L = \frac{tU_\infty}{L}, \tag{15}$$

where $t$ is the dimensional time index. Then, frequency is non-dimensionalised to Strouhal number, defined as before,

$$\mathrm{St}_L = \frac{fL}{U_\infty}. \tag{16}$$

The plots in Figure 3 and 4 give the dimensional ASD estimates and contours of AWP normalised by variance, respectively, at RF410 and RF610 as a function of $M_\infty$ and $\beta$. The ASD estimates were produced using the same parameters as discussed in Section 1. Displayed results are restricted to the range $0.001 \leq \mathrm{St}_L \leq 0.02$, and additionally for the AWP in the domain $1{,}000 \leq \tau_L \leq 25{,}000$ to avoid wavelet edge artefacts [18]. Furthermore, only AWP data at or above the 95% confidence level are plotted to highlight statistically significant features. In Figure 5, the ASD data in Figure 3 are integrated over the $0.001 \leq \mathrm{St}_L \leq 0.02$ bandwidth, and the square-root taken to give the band-limited root-mean-square (RMS) value $p_{\mathrm{RMS}}$, normalised by the value at $\beta = 0$ degrees, shown as a function of $M_\infty$ and $\beta$. It is important to clarify that this spectral cumulant is indiscriminate and does not account for the 95% confidence levels present in Figure 4. The volume of data presented in Figures 3 to 5 aligns with the authors' intention of exposing the LF bandwidth; though some observations and interpretations will be given here, the task of further scrutiny is left to the reader, for brevity.

Consistent with observations in [1], the zero-yaw case exhibits the most severe pressure fluctuations near the cavity rear lip for $M_\infty > 0.5$, and these augment as Mach number increases. Furthermore, due to symmetry, these fluctuations appear consistent across RF410 and RF610 as their AWP contours are remarkably similar, though the magnitudes are marginally larger at the RF410 location, potentially indicating a slight bias of the source mechanism towards one side of the cavity like observed in [13]. It was estimated that a systematic error of $\sim 0.07^\circ$ was present in the cavity setting angle in [3], which probably explains this slight bias.

Gaps between statistically significant peaks in normalised AWP do not imply source deactivation; they indicate fluctuations indistinguishable from background noise (null hypothesis $H_0$) and thus not statistically significant. This interpretation provides a suitable basis for defining intermittency: in regions where wavelet quantities decrease beneath the 95% confidence level, the mode(s) is/are considered to be inactive, and vice versa. Using this definition, it is evident that the LF dynamics at $\beta = 0^\circ$ are intermittent to varying amounts: at the lowest Mach number in Figures 4a and 4e, the significant activity approximately in the range $0.005 \lesssim \mathrm{St}_L \lesssim 0.01$ is highly intermittent and non-stationary (i.e. exhibiting mode-switching behaviour). The convective time-scales of these peaks span on the order $\mathcal{O}(\Delta\tau_L) \sim 300$, which at $M_\infty = 0.5$ translates to $\mathcal{O}(\Delta t) \sim 0.4$ s in dimensional time. However, at higher Mach numbers in Figures 4b to 4d and 4f to 4h, LF intermittency is significantly diminished, and large-scale fluctuations in the $0.001 \lesssim \mathrm{St}_L \lesssim 0.005$ bandwidth persist for much longer convective time-scales. Interestingly, these strong fluctuations drive the power in this bandwidth upwards by 2 orders of magnitude over the Mach number range, while spectral content for $\mathrm{St}_L > 0.01$ is significantly less amplitude modulated (Figure 3). This appears to be a unique feature of the zero-yaw case, not appearing in any other ASDs for non-zero yaw as Mach number increases. The nature and severity of these zero-yaw pressure fluctuations in the time domain (see [1]) justifies the forthcoming analysis in Section 3.2.

The disparate LF dynamics between RF410 and RF610 in Figure 4, as cavity yaw angle is increased, are notable. For instance, there are almost no significant peaks in AWP for $25^\circ \leq \beta \leq 45^\circ$ at RF610, which mildly contrasts with RF410. At $\beta = 15^\circ$ and $20^\circ$, there are significant peaks in AWP for $M_\infty = 0.5$

[4]Note that the definition of cavity yaw angle in this work is opposite to that defined formally in Henbest et al. [3].

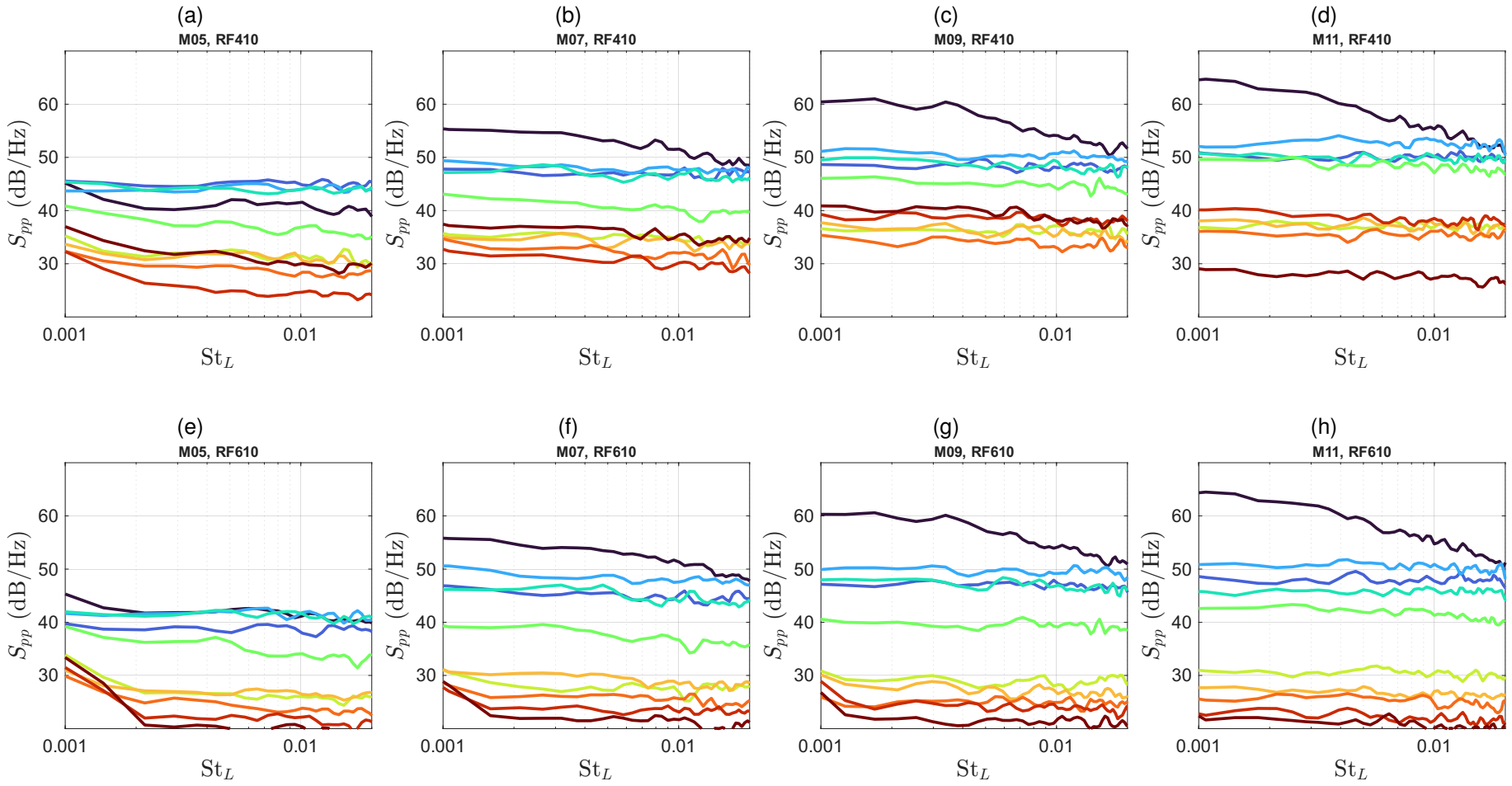



Figure 3 – $\beta = 0^\circ$ 45° in $\Delta\beta = 5^\circ$ increments. Dimensional ASDs of the $0.001 \leq \mathrm{St}_L \leq 0.02$ bandwidth as a function of $\beta$ and $M_\infty$.

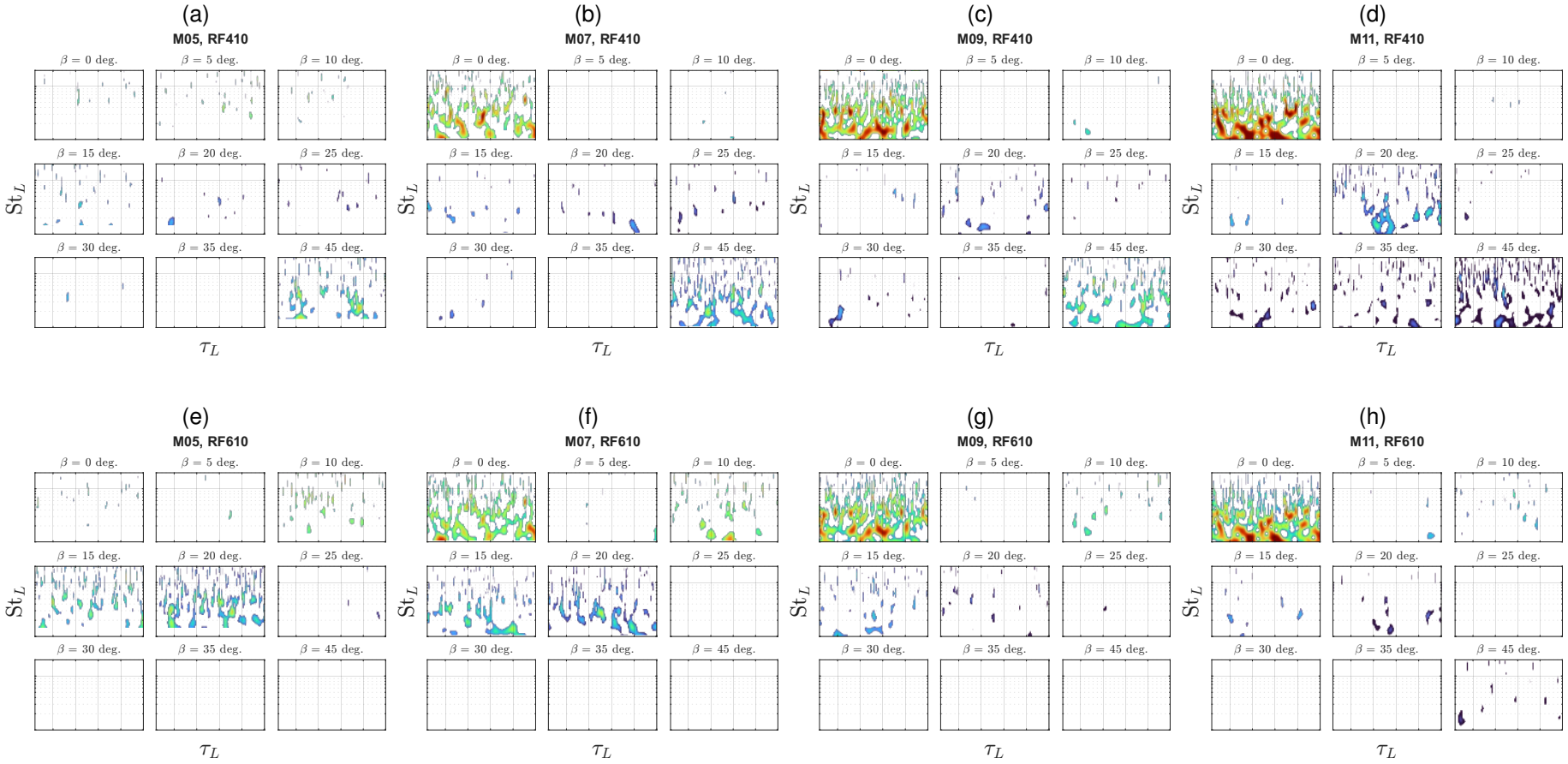



Figure 4 – Logarithmic-scale contours of $W_{XX}/\sigma_x^2$ at or above 95% confidence (Section 2.2), for sensors RF410 and RF610 as a function of Mach number and cavity yaw angle, in 1.4-dB increments (i.e. a plot range of 14 dB). Strouhal number is plotted on a logarithmic scale in the range $0.001 \leq \mathrm{St}_L \leq 0.02$, and convective time is plotted on a linear scale in the domain $1,000 \leq \tau_L \leq 25,000$.

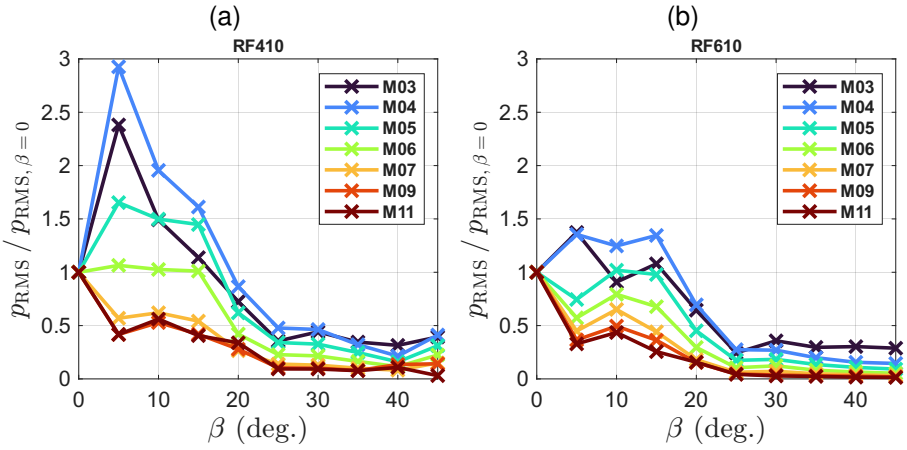



Figure 5 – Band-limited $p_{\mathrm{RMS}}$ fluctuations obtained by integrating the ASD over $0.001 \leq \mathrm{St}_L \leq 0.02$, plotted as a function of $\beta$ and $M_\infty$ and normalised by the value at $\beta = 0°$. Note: additional data at $M_\infty = 0.3$, $0.4$ and $0.6$ are presented to clarify the trend at $M_\infty = 0.5$.

and $0.7$ at RF610, but relatively few at RF410; however, this observation reverses at $M_\infty = 0.9$ and $1.1$. This indicates an appreciable sensitivity of this LF bandwidth near the cavity rear lip to changes in oncoming flow parameters. For $\beta > 0°$, there are several notable effects as illustrated in Figure 6:

1. Stream-wise and cross-stream components of oncoming flow velocity appear, with the latter becoming more prominent as $\beta$ is increased.

2. The 'effective' cavity $L/D$ ratio that each sensor 'sees', denoted as $(L/D)_{\mathrm{eff}}$, differs with respect to the oncoming flow vector.

3. The ratio of boundary-layer thickness to cavity length, $\delta/L$, differs with respect to RF410 and RF610 and the edge of the cavity, denoted as $(\delta/L)_{\mathrm{eff}}$. The Rossiter modes are known to be very sensitive to this parameter (e.g. [2] and references therein); however, its effect on the LF cavity dynamics is not well understood.

4. The Rossiter mode feedback path between the cavity front and rear walls is effectively severed; however, it is possible that a cavity side-wall to rear-wall feedback mechanism arises in its place [14].

Using a sensor on the cavity floor and adjacent to BF108 (Figure 2), Henbest et al. [3] evaluated changes to the Rossiter modes as a function of $\beta$, and observed frequency-magnitude modulations in modes 1 and 2 as $\beta$ approached the cavity diagonal angle ($11.3°$ in the case of the $L/D = 5$ cavity). For $M_\infty > 0.5$, there is a local peak in $p_{\mathrm{RMS}}$ at $\beta = 10°$ in Figure 5, indicating that the LF bandwidth may also modulate when $\beta \approx \arctan(W/L)$, where $W$ is cavity width. This tendency is also reflected in Figures 4b to 4d and 4f to 4h, where for $\beta = 5°$ there are almost no significant peaks in AWP over the entire sample period, but at $\beta = 10°$ more peaks are distinguishable from the background spectrum—marginally for RF410, but moreso at RF610. There is also a clear Mach dependence of this LF modulation, where $p_{\mathrm{RMS}}$ at $\beta = 10°$ generally diminishes as Mach is increased, and the reduction is much more significant at RF410 compared to RF610. However, this behaviour is not as evident in the AWP data in Figure 4.

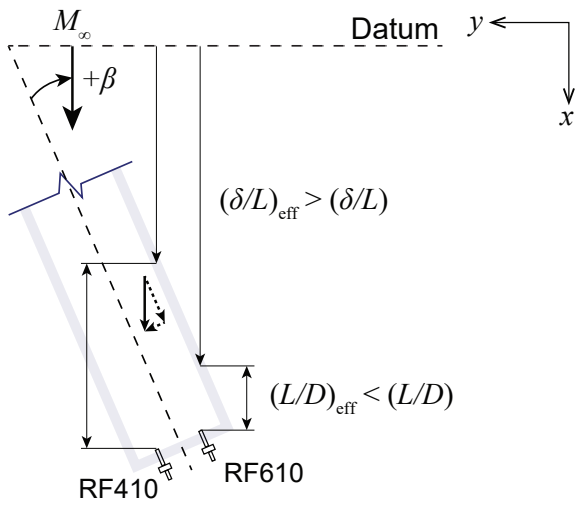



Figure 6 – Illustration of cavity yaw angle and the effects with respect to sensors RF410 and RF610. Note that the schematic is not to scale.

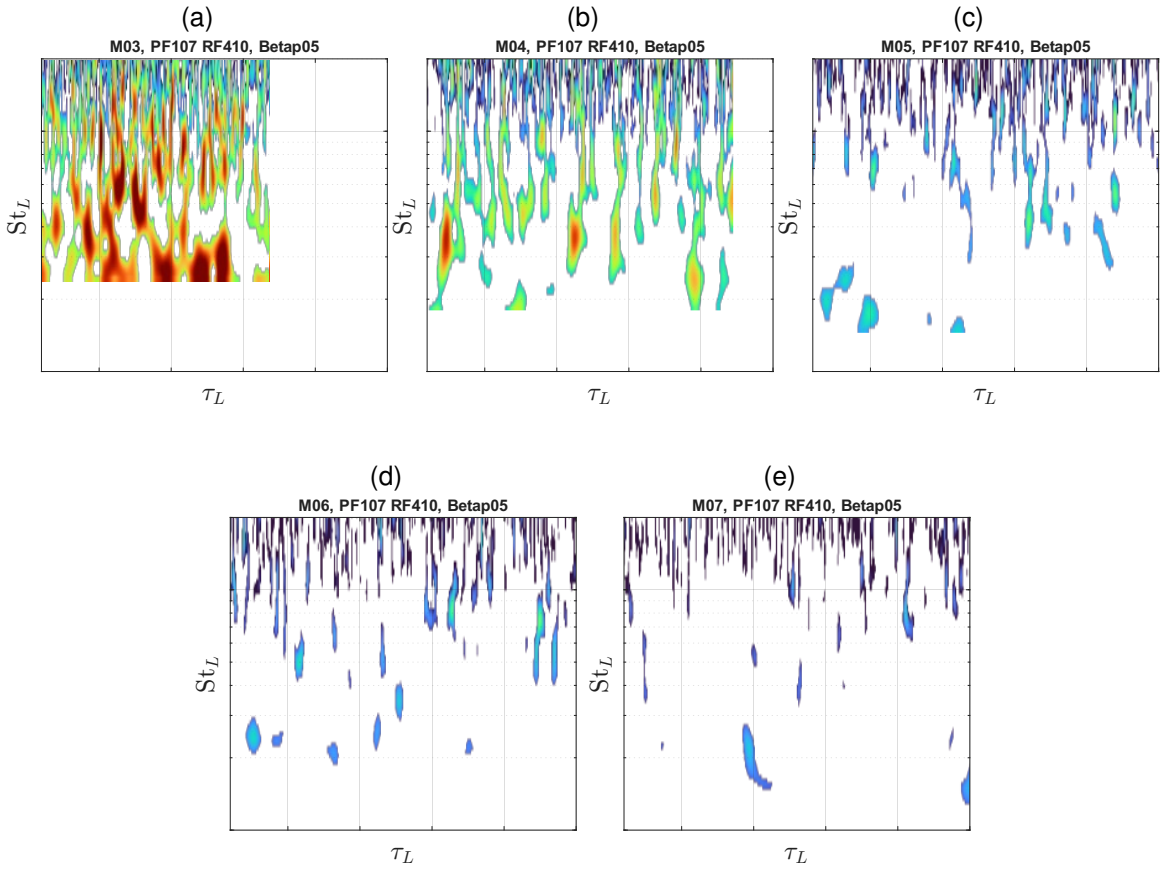



Figure 7 – Logarithmic-scale contours of $W_{XY}/\sigma_x\sigma_y$ at or above 95% confidence (Section 2.2), between PF107 and RF410 as a function of Mach number and at $\beta = 5^\circ$ ('Betap05'), in 1.4-dB increments (i.e. a plot range of 14 dB). Strouhal number is plotted on a logarithmic scale in the range $0.001 \leq \text{St}_L \leq 0.02$, and convective time is plotted on a linear scale in the domain $1,000 \leq \tau_L \leq 25,000$.

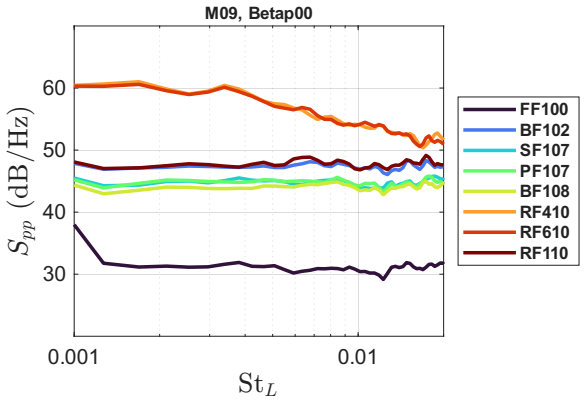



Figure 8 – Dimensional ASDs of the $0.001 \leq \mathrm{St}_L \leq 0.02$ bandwidth as a function of cavity location, at $M_\infty = 0.9$ and $\beta = 0^\circ$ ('Betap00').

The most interesting feature highlighted in Figure 5 is the behaviour at $\beta = 5^\circ$ for the RF410 sensor. Initially, it was thought that the data point at $M_\infty = 0.5$ might be an outlier, so additional data from [3] at $M_\infty = 0.3,\ 0.4$ and $0.6$ were added to contextualise the $M_\infty = 0.5$ data. This reveals a highly Mach-sensitive mechanism that peaks at $M_\infty = 0.4$, and collapses for $M_\infty > 0.6$, making it clear that the trend at $M_\infty = 0.5$ is both consistent and is associated with a genuine cavity flow feature. Similarly to $\beta = 10^\circ$, there are very few significant peaks in AWP (Figure 4a) for $\beta = 5^\circ$. This is due to the 1) normalisation by the wide-band variance, and 2) significance test against a background spectrum with $\gamma$ chosen based on the signal properties, which indicates that the amplification or attenuation of $p_{\mathrm{RMS}}$ for these cavity yaw angles with Mach number is due to a broadband mechanism, such as energy or momentum transfer, rather than temporally localised, impulsive fluctuations such as those observed at $\beta = 0^\circ$.

To further investigate the nature of the LF mechanism at RF410 and $\beta = 5^\circ$, contours of variance-normalised CWP computed between RF410 and PF107 are displayed in Figure 7 for $0.3 \leq M_\infty \leq 0.7$ where the largest variation in $p_{\mathrm{RMS}}$ at RF410 exists. Sensor PF107 was chosen based on its proximity to RF410, and hence the potential to correlate any LF dynamics occurring in the corner of the cavity at $\beta = 5^\circ$ (Figure 2). Constraining the range of $\mathrm{St}_L$ and domain of $\tau_L$ on the plot axes means that the time-frequency content modulates in dimensional space; this is why the CWP maps do not fill the plot area at lower Mach numbers. Again, similarly to the AWP contours in Figure 4, only statistically significant peaks in CWP are shown. At $M_\infty = 0.3$, very prominent peaks in CWP are evident across the range of $\mathrm{St}_L$, evincing the presence of a broadband flow structure that comprises high-amplitude fluctuations and is spatially correlated across the cavity port and rear walls. Many of these peaks persist when $M_\infty = 0.4$, where $p_{\mathrm{RMS}}$ is a maximum in Figure 5, but they are more intermittent and lower magnitude, indicating progressive decorrelation or destructive interference of the source mechanism between PF107 and RF410. Further increases to $M_\infty$ see an almost complete decorrelation of any significant peaks in CWP, corresponding to a reduction in $p_{\mathrm{RMS}}$ at RF410. In aggregate, the AWP data in Figure 4, $p_{\mathrm{RMS}}$ data in Figure 5, and CWP data in Figure 7 suggest that a unique and significant corner-based flow structure exists near RF410 and PF107 for this cavity geometry at $\beta = 5^\circ$, which is more unstable at lower Mach numbers, but stabilises as the oncoming flow momentum increases. Even in the comprehensive review of cavity flow dynamics by Hamilton-Smith et al. [14], this specific feature has yet to be elucidated in any detail; however, it is likely related to the asymmetric flow state realised on the cavity rear lip for non-zero yaw angles as per [13].

## 3.2 Cavity Spatial Dependence

It is also important to understand spatial variations of the LF bandwidth throughout the cavity. Dimensional ASD curves and contours of AWP as a function of cavity location are given in Figures 8 and 9 respectively, at $M_\infty = 0.9$ and $\beta = 0^\circ$. There are 4 distinct curve groupings visible in the ASDs, in order of descending spectral power: 1) near the cavity rear lip (RF410 and RF610) as before, 2) near the fore cavity on the floor and on the rear wall (BF102 and RF110), 3) near the aft cavity (SF107, PF107 and BF108), and 4) the front wall (FF100). These groupings were also typical of the cavity at

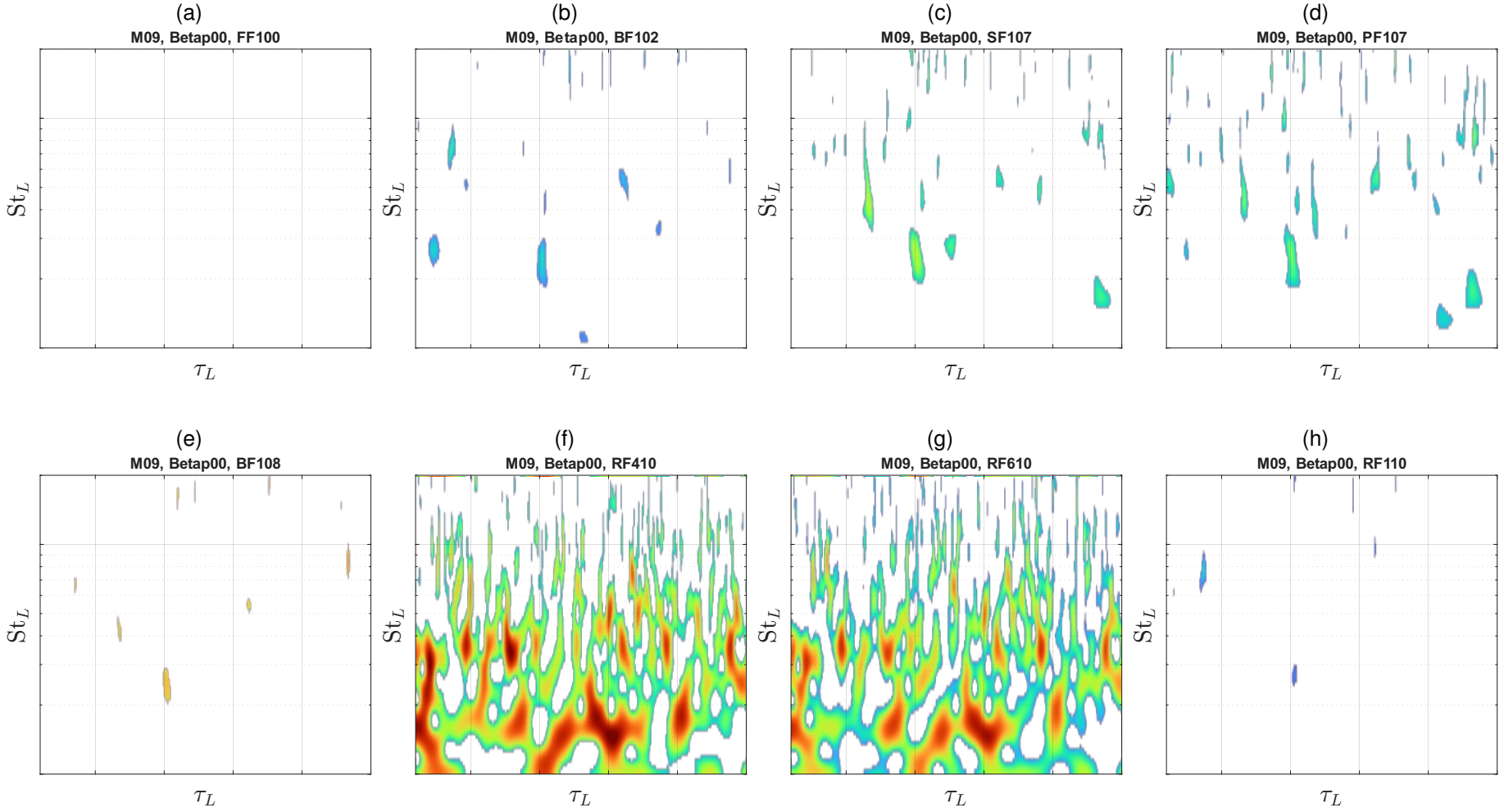



Figure 9 – Logarithmic-scale contours of $W_{XX}/\sigma_x^2$ at or above 95% confidence (Section 2.2), as a function of cavity location (Figure 2) at $M_\infty = 0.9$ and $\beta = 0^\circ$ ('Betap00'), in 1.4-dB increments (i.e. a plot range of 14 dB). Strouhal number is plotted on a logarithmic scale in the range $0.001 \leq \mathrm{St}_L \leq 0.02$, and convective time is plotted on a linear scale in the domain $1,000 \leq \tau_L \leq 25,000$.

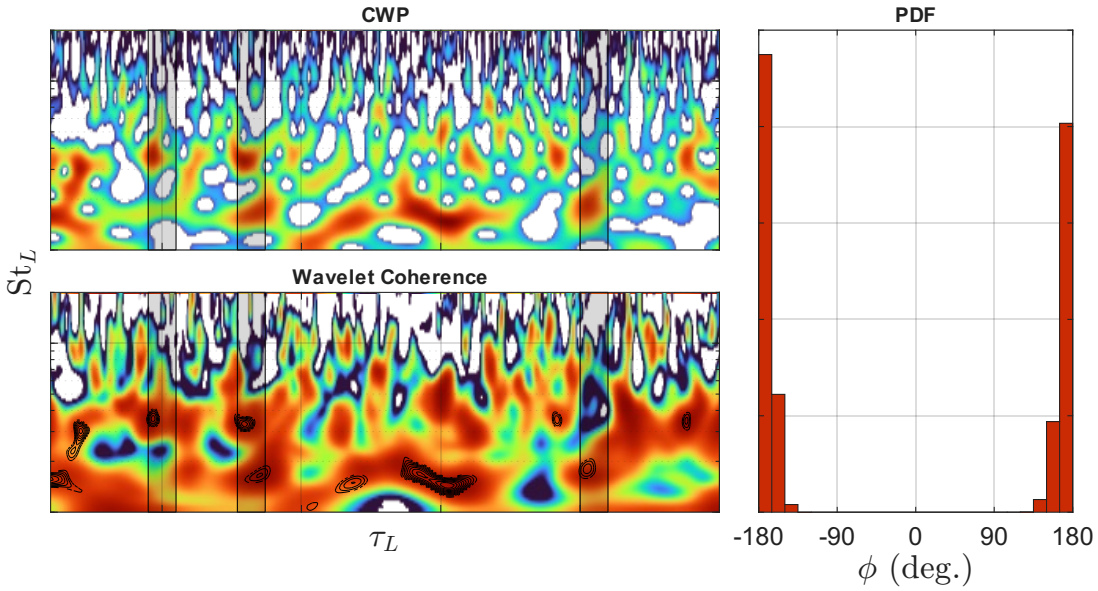



Figure 10 – **CWP:** Logarithmic-scale contours of $W_{XY}/\sigma_x\sigma_y$ at or above 95% confidence (Section 2.2), between RF610 and RF410, in 1.4-dB increments (i.e. a plot range of 14 dB). **Wavelet Coherence:** Linear-scale contours of $R^2$ at or above 95% confidence (Section 2.2), between RF610 and RF410, in the range $0.8 \leq R^2 \leq 1$. The black iso-lines denote regions where $R^2 \geq 0.9$ and $(W_{XY}/\sigma_x\sigma_y) \geq 0.5\,(W_{XY}/\sigma_x\sigma_y)_{\max}$. **PDF:** PDF plot of $\arg(W_{xy})$, $\phi$, between RF610 and RF410 where $R^2 \geq 0.9$ and using a bin width of $15°$. Strouhal number is plotted on a logarithmic scale in the range $0.001 \leq \mathrm{St}_L \leq 0.02$, and convective time is plotted on a linear scale in the domain $1{,}000 \leq \tau_L \leq 25{,}000$. The shaded regions denote regions of interest in Figure 11.

$M_\infty = 0.7$ and $0.9$, though at $M_\infty = 0.7$ ASDs from BF102, RF110, SF107, PF107 and BF108 exhibited almost complete collapse, and at $M_\infty = 1.1$ these 2 groupings separated further. This indicates a Mach sensitivity of the flow mechanism driving LF pressure fluctuations in these cavity locations, and from the AWP data in Figure 9 it is evident that these are broadband with very few significant peaks occurring over the convective period. In fact, the only significant and largely non-intermittent LF activity occurs at RF410 and RF610, as observed previously.

There are almost no discernible LF cavity dynamics occurring on the front wall, but on the cavity floor near the front (BF102) there are broadband fluctuations nearly 2 orders of magnitude greater, which could indicate the presence of a highly localised flow structure. Bacci et al. [16] for a cavity $L/D = 5.66$ and $M_\infty = 0.85$ with zero yaw showed 3 distinct vortical structures within the cavity, a primary streamwise vortex centred at roughly $x/L = 0.4$ driving 2 secondary vortices situated around $x/L = 0.05$ and $0.9$. Between the foremost secondary vortex and the primary vortex exists a low-pressure region where a local separation node exists, at roughly the location of BF102. The elevated broadband power observed at this location most likely indicates transient movement of this separation node via distortion or translation of the primary and foremost secondary vortices.

As mentioned in Section 3.1, the similarity in AWP maps between RF410 and RF610 potentially indicates a spatio-temporal relationship. Turpin et al. [13] showed for an open-transitional cavity at $M_\infty = 1.5$ that a bi-stable, high-amplitude pressure fluctuation was evident near the cavity rear lip, which at zero yaw exhibited seemingly random snap-through events from one side of the cavity to the other, at Strouhal numbers 2 orders of magnitude below the first Rossiter mode ($\mathrm{St}_L \sim 0.001$ to $0.002$). Basley et al. [12] also observed similar LF fluctuations near the rear lip, but on a two-dimensional cavity at very low Reynolds and Mach number in a water tunnel facility. Here, both the CWP and wavelet coherence between RF410 and RF610 are examined to determine whether this mechanism also appears. Additionally, complex-valued $W_{xy}$ reveals time-frequency phase information between RF410 and RF610—whether phase-locking occurs, and if so, whether in-phase, anti-phase, or otherwise. In Figure 10, the CWP, wavelet coherence, and a PDF of the argument of $W_{xy}$ (i.e. phase angle $\phi$) are shown.

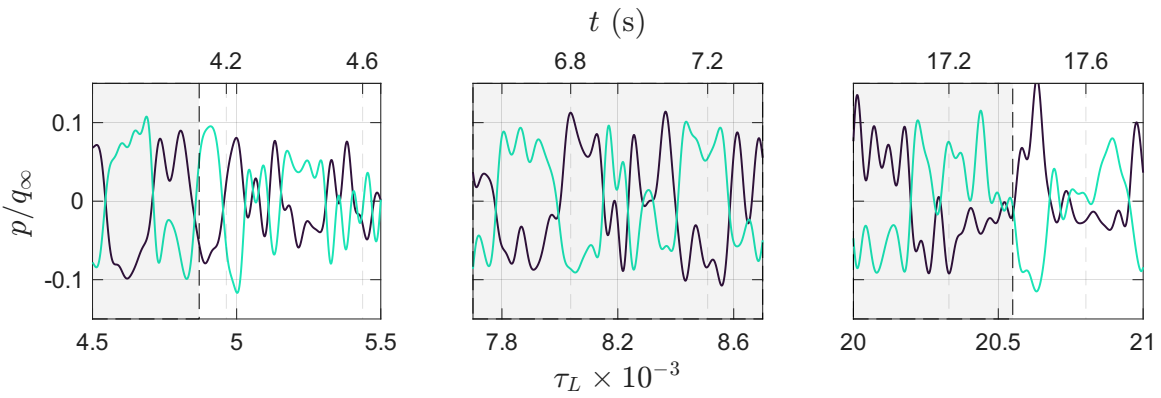



Figure 11 – Inverse wavelet transform of the $0.001 \leq \mathrm{St}_L \leq 0.02$ bandwidth for RF610 and RF410, at $M_\infty = 0.9$ and $\beta = 0°$, for the 3 windows of interest highlighted in Figure 10. $p$ is non-dimensionalised by $q_\infty$, and the gray regions denote the persistence times of the black iso-lines within each of the windows of interest in Figure 10 where $R^2 \geq 0.9$ and $(W_{XY}/\sigma_x\sigma_y) \geq 0.5\,(W_{XY}/\sigma_x\sigma_y)_{\max}$. Dimensional time is shown for reference.

Several threshold functions are used to clarify the trends in Figure 10. First, while the contour maps of CWP and wavelet coherence appear qualitatively similar, it is important to note that regions of high CWP can correspond to regions of low coherence, and vice versa. The most significant regions are those with both high CWP and coherence, so these are denoted by black iso-lines overlaid on the coherence map, corresponding to regions where $R^2 \geq 0.9$ and normalised CWP greater than or equal to 50% of its maximum global value. Second, the PDF of $\phi$ is computed only in regions where $R^2 \geq 0.9$, to ensure that detected high-coherence events are phase-locked. This shows that the highly coherent events are primarily anti-phase, with $\phi > 150°$ or $\phi < -150°$, suggesting organised span-wise motion of a pressure front at multiple frequencies contained within the LF bandwidth. It is noted that the high-power, high-coherence events occur aperiodically at $\mathrm{St}_L \sim 0.0015$ and $\sim 0.0033$, which are approximately harmonic multiples. The persistence times of these events (i.e. the width of the black iso-line regions in Figure 10) are, on average, $\Delta\tau_L \sim 595 \pm 250$ convective units (excluding the long-duration peak at $\tau_L \sim 13{,}000$, which persists for $\sim 2{,}700$ units). At $M_\infty = 0.9$, this translates to $\Delta t \sim 0.5 \pm 0.21$ s in dimensional time.

Utilising the inverse wavelet transform [18] and band-pass filtering between $0.001 \leq \mathrm{St}_L \leq 0.02$ reveals the time-domain behaviour of the RF410 and RF610 LF pressure fluctuations, $p$, here non-dimensionalised by free-stream dynamic pressure, $q_\infty$. In Figure 11, 3 temporal regions of interest are shown that correspond with the 3 regions highlighted in Figure 10. In general, the low-pressure peaks at one span-wise location correspond to high-pressure peaks at the opposite span-wise location, evincing the predominantly anti-phase behaviour and confirming the span-wise oscillations of the pressure front as reported in [13]. The anti-phase locking behaviour appears at multiple frequencies, especially in the windows of time where high-power, high-coherence events persist. Also, some of these static pressure fluctuations are as large as $\gtrsim 20\%$ of $q_\infty$ over short intervals, which is an appreciable deviation in pressure-based loading.

Finally, to demonstrate the LF aperiodicity compared to the dominant Rossiter modes, a time-marching computation of $p_{\mathrm{RMS}}$ was performed, at RF410 for the $0.001 \leq \mathrm{St}_L \leq 0.02$ bandwidth, as well as for a summation of the second and third Rossiter modes[5], using $\Delta\tau_L = 10$, $100$ and $1{,}000$ as the sliding window length. This computation is performed as follows: at each convective time-step $\tau_L$, $p_{\mathrm{RMS}}$ is computed over the previous $\Delta\tau_L$ time-steps for both time traces (i.e. the LF time trace and summation of the second and third Rossiter mode time traces). Then, the time-step advances by $\tau_L + 1$ and the computation is repeated and so on, until $t_s = \tau_{L_{\max}} L/U_\infty$ is reached. The results are displayed in Figure 12, where large excursions in $p_{\mathrm{RMS}}$ of the LF bandwidth reveals its appreciable volatility compared with the dominant Rossiter modes, which do not vary significantly in $p_{\mathrm{RMS}}$. As expected, larger

[5]These are the dominant modes at these oncoming flow conditions as noted by Henbest et al. [3], the band-passed time traces of which were obtained using the inverse wavelet transform as with the LF time trace.

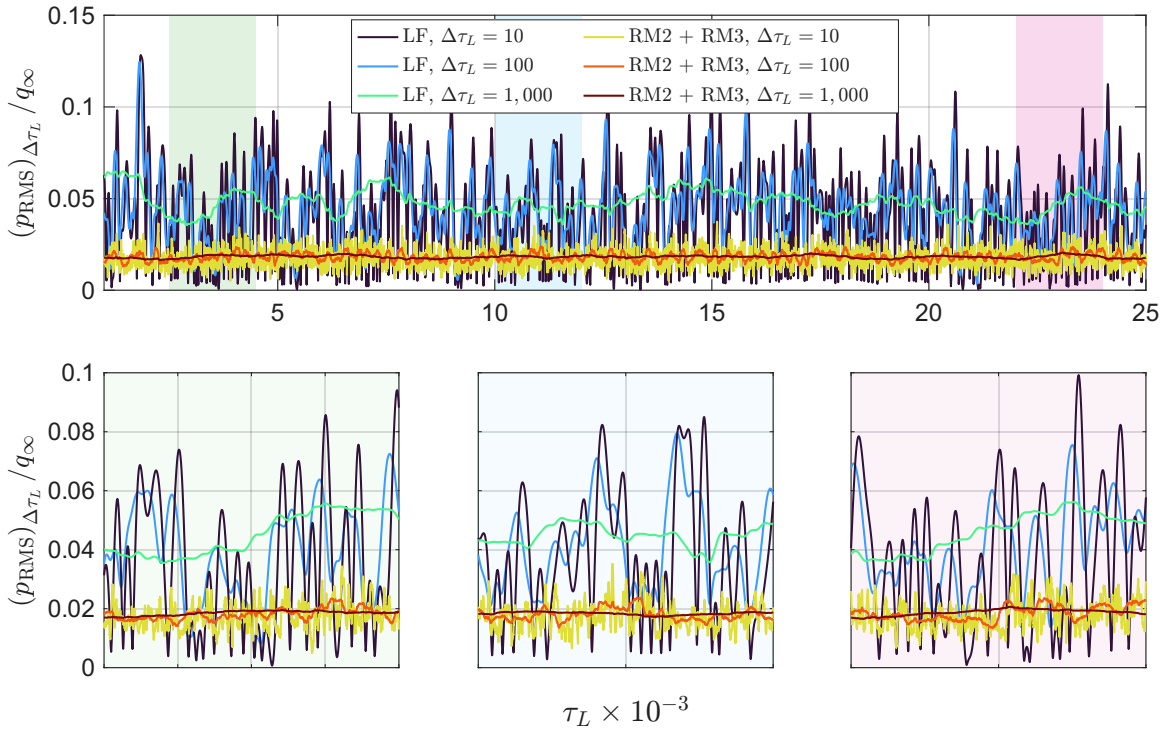



Figure 12 – Time-marching $p_{\mathrm{RMS}}$ computation over the $0.001 \leq \mathrm{St}_L \leq 0.02$ bandwidth (LF), and a summation of Rossiter modes 2 and 3 (RM2 + RM3) obtained using the inverse wavelet transform, for RF410 at $M_\infty = 0.9$ and $\beta = 0°$. $p_{\mathrm{RMS}}$ is non-dimensionalised by $q_\infty$, and 3 sliding window lengths of $\Delta\tau_L = 10$, $100$ and $1,000$ are used. Three arbitrary regions of interest are highlighted to clarify trends in LF and RM2 + RM3 with varying $\Delta\tau_L$.

convective time windows lead to a reduced volatility in both bandwidths. The flight-scale simulation data of [1] revealed that typical shear-layer traverse times for the cavity-released store were on the order $\mathscr{O}(\Delta\tau_L) \sim 10$, which by the data in Figure 12 suggests that if significant LF content is present, the pressure loading exerted on the store near the cavity could exhibit large temporal aberrations in amplitude. This potentially leads to drastic changes in the initial conditions of the store at release time, ultimately diminishing post-release trajectory repeatability.

## 4 Discussion

The empty-cavity data in [2, 3, 13] all revealed qualitatively consistent trends in spatial variations of the cavity Rossiter-mode amplitudes in the stream-wise direction—with maximum amplitudes observed at the aft cavity—due to the standing-wave characteristics of the acoustic feedback mechanism. By comparison, the data and analyses presented in Section 3 show that the aft-cavity LF bandwidth contains high-amplitude and significant fluctuations, which persist over long periods of time. However, data in Figures 8 and 9 also reveal significant, albeit highly intermittent, LF fluctuations at other cavity locations. For example, at all cavity locations except FF100 in Figure 9, there is significant activity at $\tau_L \sim 10,000$, but its nature varies depending on cavity location. At RF410 and RF610 for this time instance, there is a high-magnitude peak at $\mathrm{St}_L \sim 0.001$ and significant power across most of the LF bandwidth, while at the remaining locations an approximately co-located peak occurs in the $0.002 \lesssim \mathrm{St}_L \lesssim 0.003$ bandwidth. Similar occurrences also arise at other spatio-temporal locations, and these suggest the existence of globally impulsive events, originating on the cavity rear lip, which excite multiple aero-acoustic modes simultaneously throughout the cavity. Basley et al. [12] observed amplitude modulation and nonlinear energy transfer from a LF mechanism—a centrifugal instability—observed near the cavity floor, to Rossiter modes within the cavity shear layer; however, this is unlikely related to the impulsive mechanism suggested here. Further investigations are required at more representative Mach numbers and cavity geometries.

It was discovered (somewhat unintentionally) in the experiments of [13] that a small cavity yaw angle,

$\beta \sim 3°$, largely attenuated the LF oscillation attributed to a bi-stable pressure front, forcing it to one side of the cavity rear lip. The wavelet data in Figure 4 corroborate this finding at the smallest $\beta$ studied ($5°$), where nearly all significant peaks in AWP disappear from the rear lip for $M_\infty \geq 0.7$; but at lower Mach numbers it is clear from Figure 5 that a substantial Mach sensitivity of the LF bandwidth appears for $\beta \leq 25°$. Furthermore, significant peaks in AWP reappear as $\beta$ transitions past $10°$, or close to the cavity diagonal of $11.3°$ in the present study. At some Mach numbers, more significant fluctuations appear on the port aft cavity (RF410), while for other Mach numbers the fluctuations are more concentrated on the starboard aft cavity (RF610), and no discernible patterns in terms of intermittency are evident. The band-limited RMS amplitudes in Figure 5 do show that the port aft cavity generally experiences larger broadband fluctuation levels relative to the starboard side, which appears consistent with the asymmetric flow state observed in [13], except that the global definition of $\beta$ in the axis system was not defined, making direct comparison difficult. Furthermore, Mach and yaw sensitivities were not available in [13] because only 1 Mach number and cavity yaw angle were examined in detail. Future flow visualisation studies at different cavity yaw angles and locations would greatly strengthen any further comparisons between the present study, and that of [13].

The spectral information in Figure 1 was available at $t_s = 40$ s as opposed to $1$ s. At $M_\infty = 0.9$ for the cavity studied here, a sample period of $1$ s corresponds to $\mathscr{O}(\Delta\tau_L) \sim 1{,}000$, which was of order the maximum physical run-time available ($\tau_L = 904$) for pressure data obtained in SR-CFD simulations of the cavity at $M_\infty = 1.5$ by [13]. The SR-CFD simulations, unlike the experiments in [13], were run with $\beta = 0°$ as a prescribed condition with zero uncertainty, so that the bi-stable LF activity on the cavity rear lip could be observed. Despite this, the statistical disadvantages of relatively short sample periods were evident: only 2 span-wise fluctuations at $\mathrm{St}_L \sim 0.003$ were resolved, leading to a 1) reduced resolution bandwidth of spectral quantities, and a 2) lack of statistical power within this bandwidth. Indeed, a temporal window size of $\Delta\tau_L = 1{,}000$ in Figure 12 revealed that a notable volatility in the LF bandwidth $p_{\mathrm{RMS}}$ remained, which suggests that for complete characterisation, longer sample periods are required of SR-CFD simulations (or wind-tunnel data for that matter). As a first measure of required sample times, a convergence test on variability in $p_{\mathrm{RMS}}$ of the LF bandwidth as a function of $\Delta\tau_L$, using a time-marching computation such as that proposed in this work, could be employed as a monitor variable during simulations or experiments, similar in principle to the mature cavity computation proposed by Jolly et al. [8] for Rossiter modes.

Lastly, it should be reiterated that, even at temporal scales relevant to cavity-released stores, which are typically an order of magnitude less than SR-CFD run-times, the data in Figure 12 suggests that the Rossiter-mode RMS amplitudes are remarkably stable; rather, it is the LF bandwidth that contains fluctuation periods of most relevance to store release time-scales. As expressly noted by Marshall et al. [1], these fluctuations potentially affect the trajectory repeatability of a cavity-released store, especially in cases where the ratio of store inertial or aero-stability forces to cavity-borne pressure forces is low. As modern aerial combat platforms demand greater stealth and payloads become progressively smaller, understanding the wide-band aero-acoustic environment of cavities—not just Rossiter modes—is essential.

## 5 Concluding Remarks

This study examined LF dynamics in an empty rectangular cavity ($L/D = 5$) across a range of Mach numbers and yaw angles. The dataset, originally collected by Jones et al. [2] and Henbest et al. [3], focused on the spatio-temporal behaviour of Rossiter modes. Here, it was re-analysed to investigate LF characteristics and their potential role in cavity store trajectory non-repeatability [1]. Further work is needed to link observed surface pressure phenomena with time-resolved off-surface flow features, as well as to assess more flight-representative cavity geometries. Furthermore, it is concluded that:

1. The strongest LF pressure fluctuations occur at the aft cavity lip at zero yaw. They are broadband ($0.001 \leq \mathrm{St}_L \leq 0.02$) and can rival or exceed the dominant Rossiter mode in spectral power. Their strong coherence and anti-phase behaviour across span-wise sensors indicate a combination of span-wise shear-layer oscillation [13] and shear-layer impingement [12].

2. The effect of cavity yaw angle on the LF bandwidth is still not fully understood. However, it is clear that fluctuations in the LF bandwidth are significantly Mach sensitive for $\beta \leq 25°$ given

this cavity geometry, and the asymmetric flow state initially documented in [13] for small $\beta$ is observed in the present work.

3. At convective time scales comparable to the shear-layer residence time of cavity-released stores, Rossiter-mode RMS amplitudes are notably stable. In contrast, the LF bandwidth RMS amplitude varies significantly, creating highly transient initial conditions for released stores and potentially reducing trajectory repeatability.

4. To more fully characterise the LF bandwidth, longer sample periods are required of SR-CFD simulations or experimental data. A first-order method to assess the required sample period has been suggested by the authors.

## 6 Contact Author Email Address

Please direct all inquiries to the corresponding author: Jesse.McCarthy@defence.gov.au

## 7 Copyright Statement

The authors confirm that they, and/or their company or organisation, hold copyright on all of the original material included in this paper. The authors also confirm that they have obtained permission, from the copyright holder of any third party material included in this paper, to publish it as part of their paper. The authors confirm that they give permission, or have obtained permission from the copyright holder of this paper, for the publication and distribution of this paper as part of the ICAS proceedings or as individual off-prints from the proceedings.

## References

[1] Marshall C, McCarthy J, Hale E, and Jolly B. On Some Proposed Modifications to the J-factor Store Trajectory Repeatability Predictor. *AIAA-2026-4280*, June 2026.

[2] Jones M, Henbest S, Watmuff J, and Blandford A. Aeroacoustic resonance in a rectangular cavity: Part 1 effect of Mach number and Reynolds number. In *18th Australasian Fluid Mechanics Conference*, Launceston, Australia, 2012.

[3] Henbest S, Jones M, Blandford A, and Watmuff J. Aeroacoustic resonance in a rectangular cavity: Part 2 effect of yaw and of leading and trailing edge angles. In *18th Australasian Fluid Mechanics Conference*, Launceston, Australia, 2012.

[4] Jolly B, Aziz W, Clapp A, and Amour A. J-factor Theory & Explanation for Predicting Store Trajectory Repeatability. *AIAA-2022-3451*, June 2022.

[5] Das A and Marzocca P. A Data-driven Reduced Order Model for Trajectory Prediction of Cavity Store Release. In *21st Australian International Aerospace Congress*, Melbourne, Australia, 2025.

[6] Coley C and Lofthouse A. Correlation of Weapon Bay Resonance and Store Unsteady Force and Moment Loading. *AIAA-2012-0415*, January 2012.

[7] Rossiter J. Wind-Tunnel Experiments on the Flow over Rectangular Cavities at Subsonic and Transonic Speeds. *Aeronautical Research Council Reports and Memoranda*, 145(24):44, 46, 1966.

[8] Jolly B and Aziz W. JAIC: Cavity Acoustic-Intelligent Analysis. *AIAA-2026-1871*, January 2026.

[9] Welch P. The use of fast fourier transform for the estimation of power spectra: A method based on time averaging over short, modified periodograms. *IEEE Transactions on Audio and Electroacoustics*, AU-15(2):70 – 73, 1967.

[10] Nuttall A. Some windows with very good sidelobe behavior. *IEEE Transactions on Acoustics, Speech, and Signal Processing*, ASSP-29(1):84 – 91, 1981.

[11] Vikramaditya N and Kurian J. Nonlinear aspects of supersonic flow past a cavity. *Experiments in Fluids*, 52:1389 – 1399, 2012.

[12] Basley J, Pastur L R, Lusseyran F, Soria J, and Delprat N. Modulating effect of three-dimensional instabilities in open cavity flows. *Journal of Fluid Mechanics*, 759:546–578, 2014.

[13] Turpin A, Speth R, Sherer S, and Granlund K. Low-frequency, spanwise oscillation in a finite-width cavity at Mach 1.5. *Physics of Fluids*, 33(076102), 2021.

[14] Hamilton-Smith C, Lawson N, and Vio G. History, review and summary of the cavity flow phenomena. *European Journal of Mechanics / B Fluids*, 2024.

[15] Clapp A, Coley C, Jolly B, and Aziz A. Validating J-Factor as a Predictive Method for the Repeatability of Aircraft Store Separation from Unsteady Cavity Environments. *AIAA-2022-3452*, June 2022.

[16] Bacci D, Saddington A, and Bray D. Wavelet analysis of complex-geometry transonic cavity flows. In *8th AIAA Flow Control Conference*, Washington DC, USA, 2016.

[17] Farge M. Wavelet transforms and their applications to turbulence. *Annual Review of Fluid Mechanics*, 24:395 – 458, 1992.

[18] Torrence C and Compo G. A practical guide to wavelet analysis. *Bulletin of the American Meteorological Society*, 79(1):61 – 78, 1998.

[19] McCarthy J and Lee S-K. Wavelet coherence analysis of fluctuating surface pressure on a hemispherical protuberance. In *21st Australasian Fluid Mechanics Conference*, Adelaide, Australia, 2018.

[20] McCarthy J, Giacobello M, and Lam S. Wavelet coherence of surface pressure fluctuations due to von karman vortex shedding near a hemispherical protuberance. *Experiments in Fluids*, 60(3), 2019.

[21] Torrence C and Webster P. Inter-decadal changes in the enso—monsoon system. *Journal of Climate*, 12:2679 – 2690, 1999.

[22] Bendat J and Piersol A. *Random Data: Analysis and Measurement Procedures*. John Wiley & Sons, 2010.

[23] Allen M and Smith L. Monte Carlo SSA: detecting irregular oscillations in the presence of coloured noise. *Journal of Climate*, 9:3373 – 3404, 1996.

[24] Grinsted A, Moore J, and Jevrejeva S. Application of the cross wavelet transform and wavelet coherence to geophysical time series. *Nonlinear Processes in Geophysics*, 11:561 – 566, 2004.